Roman KRÓL (iD) [1]

Analysis of the backlash in the single stage cycloidal gearbox

In this paper the analysis of backlash influence on the spectrum of torque at the output shaft of a cycloidal gearbox has been performed. The model of the single stage cycloidal gearbox was designed in the MSC Adams. The analysis for the excitation with the torque and the analysis with constant angular velocity of the input shaft were performed. For these analyses, the amplitude spectrums of the output torque for different backlashes was solved using FFT algorithm. The amplitude spectrums of the combined sine functions composed of the impact-to-impact times between the cycloidal wheel and the external sleeves were computed for verification.

The performed studies show, that the backlash has significant influence on the output torque amplitude spectrum. Unfortunately the dependencies between the components of the spectrum and the backlash could not be expressed by linear equations, when vibrations of the output torque in the range of (350 Hz – 600 Hz) are considered.

The gradual dependence can be found in the spectrum determined for the combined sine functions with half-periods equal impact-to-impact times. The spectrum is narrower for high values of backlash.

1. Introduction

Contemporary works in the cycloidal gearbox engineering concern the aspects of dynamics [1, 2], stress analysis [3] or kinematical and dynamical modeling on the basis of multibody analysis [4, 5]. A few works [6, 7] concern kinematic errors and contact analysis. Nonlinear characteristics of the kinematical and dynamical phenomena in the cycloidal gearbox allow for a complex theoretical analysis. The

✉ Roman Król, e-mail: r.krol@uthrad.pl

[1]Faculty of Mechanical Engineering, Kazimierz Pulaski University of Technology and Humanities in Radom, Poland. ORCID:0000-0002-6279-9562

precise kinematical analysis can be performed by the application of the multibody models designed in the engineering software. The results obtained in the simulation software can be verified in the experimental measurement set up. Theoretical models defined in the mathematical software are usually very simplified and can only allow for estimating the results. In the work [2], the vibrations of the cycloidal gearbox were analyzed. There is a simplification in the mentioned model based on the assumption that the cycloidal wheel is in a permanent contact with the external sleeves. The task of building theoretical models programmed with the application of multibody dynamics and numerical methods is very laborious, because of large number of constraints and the necessity of contact modeling inside the function that integrates the motion equation. To study backlash in the cycloidal gearbox, the transient model based on the multibody dynamics is needed.

The backlash in the cycloidal gearbox was investigated in [8, 9]. In the work [10], distributed wear of the planetary gear was analyzed, and the work [11] is devoted to the topic of tooth modification in the cycloidal gearbox. The analysis of contact in the cycloidal gearbox was studied in [12]. There is a number of works concerning fault detection, which analyze planetary gearboxes with defects, but these works do not consider cycloidal gearboxes and do not directly relate to the backlash. There are the topics of removed tooth in [13–15] and damaged, scratched and cracked teeth in [16–21]. Unfortunately, the works which consider backlash in the cycloidal gearbox as a main research subject are very rare.

The aim of this work is to perform the analysis of the backlash influence on the torque at the output shaft. The motivation for studying backlash is to develop the dependencies that could improve the gearbox design process.

In this paper, the MSC Adams software was used for building the models of the cycloidal gearbox and their analysis in the scope of the backlash influence on the torque at the output shaft. The single cycloidal gearbox model consists of rigid bodies mounted on bearings and the bushings, which allow relative motions between the parts of the mechanism. The analyzed backlashes result from the design tolerances, which concern the position of external sleeves.

The following analyses were performed: 1) Solution of the discrete Fourier transform (DFT) of the output torque for different backlashes in the model loaded by the torques specified in Table 1; 2) Solution of the DFT of the output torque for different backlashes in the model with constant angular velocity of the input shaft, loaded by the output torque (Table 1); 3) Verification of the analysis (2) with the DFT solution of the combined function defined as a set of sine functions with half-periods equal to the time increments between the impacts of the cycloidal wheel into the successive external sleeves. The impact-to-impact times were determined in the model with constant angular velocity of the input shaft; 4) Comparison of the times between impacts exerted on the successive external sleeves for various backlash values; 5) Solution of the contact status versus analysis time for different backlashes in the model with constant angular velocity of the input shaft.

2. Models of the cycloidal gearbox

Each model of the cycloidal gearbox (Fig. 1) used in the analysis consists of rigid bodies: the input shaft, the output shaft, the cycloidal gears, the internal sleeves and the external sleeves. The input shaft and the output shaft are connected with the symbolic ground part through the bearings. The bearings are modeled as a radial-thrust joints, which rotate without friction. The bearings are rigid parts with infinite stiffness. The other parts (the cycloidal gears, the internal sleeves and the external sleeves) are connected through the bushings, which have radial stiffness components given in Section 3 (Table 4). The parameters of the loads are given in Table 1.
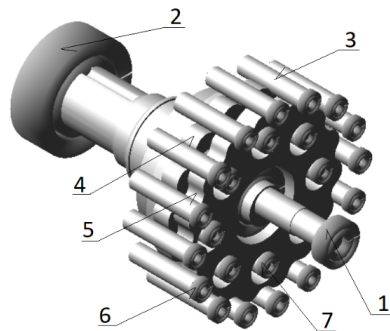

Fig. 1. The multibody dynamics model of the cycloidal gearbox designed in MSC Adams:
1 – bearing at the input shaft, 2 – bearing at the output shaft, 3 – external sleeve, 4 – internal cycloidal wheel, 5 – external cycloidal wheel, 6 – bushing at the external sleeve,
7 – bushing at the internal sleeve

Table 1. Parameters of the loads in the analyzed models

	Physical entity	Constant component [Nm]	Amplitude [Nm]	Frequency [Hz]	Velocity [rad/s]; [Hz]; [RPM]
The model loaded by the input and the output torques	Input torque	1.5	0.1	10	–
	Output torque	22.5	–	–	–
The model with the constant angular velocity of the input shaft, loaded by the output torque	Angular velocity of the input shaft	–	–	–	52.34; 8.33; 500
	Output torque	22.5	–	–	–

The difference between the models is only in the applied loads and the position of external sleeves (backlash). One type of analyses is performed with the oscillating input torque applied to the input shaft. The other type of analyses is performed with a constant angular velocity defined in the radial-thrust joint between the ground and the input shaft. The output shaft in both types of analyses is loaded by the constant

output torque simulating external load of the gearbox. In the models excited with the oscillating input torque, the frequency of the input torque was set to 10 Hz. This is the random value used for the analysis of the gearbox response (the output torque spectrum).

The request was programmed with a purpose of calculating the output torque on the basis of displacements of the internal sleeves and the forces acting on these sleeves.

The backlashes were introduced using the increase in radial position of the external sleeves (Fig. 2). In the cycloidal gearbox without backlash, the external sleeves are placed at the positions specified in the parametric equations of the cycloidal wheel (1).

$$
\begin{aligned}
u(\alpha) &= \frac{e\,z_k}{m}\cos(\alpha) + e\,\cos(z_k\,\alpha) - q\,\cos(\alpha + \gamma), \\
v(\alpha) &= \frac{e\,z_k}{m}\sin(\alpha) + e\,\sin(z_k\,\alpha) - q\,\sin(\alpha + \gamma), \\
\gamma &= \arctan\left(\frac{\sin(z_s\,\alpha)}{\dfrac{1}{m} + \cos(z_s\,\alpha)}\right),
\end{aligned}
\tag{1}
$$

where: $u(\alpha)$, $v(\alpha)$ – parametric equations of the cycloidal wheel, e – eccentricity, m – short-width coefficient, z_k – the number of external sleeves, z_s – the number of lobes, α – the argument of the parametric equations (0–2π). The values of the parameters are given in Table 2.

Table 2. Values of the parameters specified in equation (1) used in the analyses

Parameter	Description	Value
$u(\alpha)$	Horizontal coordinate	–
$v(\alpha)$	Vertical coordinate	–
α [rad]	Equation parameter	0–2π
e [m]	Eccentricity	$2.8 \cdot 10^{-3}$
z_k	Number of external sleeves	16
z_s	Number of lobes	5
m	Short-width coefficient	0.7
q [m]	Radius of the external sleeve	$6 \cdot 10^{-3}$

Six multibody dynamics models were built with the external sleeves displaced in the radial direction by 0 m (no backlash), $0.05 \cdot 10^{-3}$ m, $0.1 \cdot 10^{-3}$ m, $0.2 \cdot 10^{-3}$ m, $0.4 \cdot 10^{-3}$ m, and $0.6 \cdot 10^{-3}$ m, relative to the position in the ideal cycloidal gearbox without backlashes. For each model, the output torque was calculated and the DFT of the output torque was determined using the fast Fourier transform (FFT) algorithm.

The cycloidal gearbox model (Fig. 1) is similar to the model presented in [22]. The backlashes (Fig. 2b) were introduced using radial grid setting (Fig. 2a).
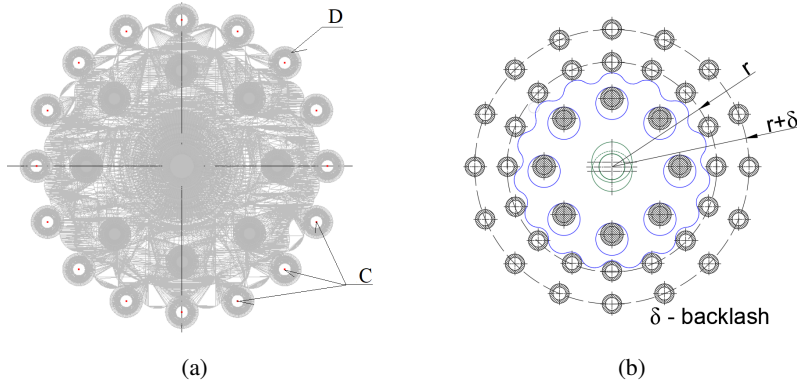

(a)   (b)

Fig. 2. The polar grid in the cycloidal gearbox model (C – the points of the grid, D – the external sleeve) (a). External sleeves were displaced from the initial position (r – zero backlash) to the grid points ($r + \delta$), where $r = ez_k/m$ (b)

The contact without friction was set up between cycloidal wheels and the sleeves. Material properties of the parts are given in Table 3.

Table 3. Material properties of the cycloidal gearbox parts. The moments of inertia are given with respect to the parts' own coordinate systems placed in the parts' mass centers

Part name	Material	Moment of inertia [kg·m^2]	Mass [kg]	Density [kg/m^3]
Input shaft	Steel	0.000014365	0.234	7801
Cycloidal wheel		0.00122748	0.599	
External sleeve		0.000000637	0.0245	
Internal sleeve		0.00000087	0.0235	
Internal pin		0.000000306	0.0245	
Output shaft		0.00150533	1.625	

3. Bushings properties

Some parts of the cycloidal gearbox (the sleeves and the cycloidal gears) are mounted on the bushings, which allow elastic deformation of the joints. Each bushing has radial stiffness of the value specified in Table 4. The analyses were performed with damping in the external sleeves' bushings specified in Table 5. For all analyses the contact damping was set to 0. The damping in contacts has an influence on the spectral characteristics of the torque at the output shaft. It is difficult to determine the accurate value of the damping in contacts. It depends on the penetration depth, which has different values in each iteration of the analysis.

Instead, the viscous damping was set in the bushings of the external sleeves for a better control of this parameter.

Table 4. Radial stiffness in bushings equivalent to the bending stiffness calculated
in the Finite Element Model of the given part

Bushing	Stiffness [N/m]
Between the internal sleeve and the internal pin	12 000 600
Between the external sleeve and the ground	200 000 000
Between the external cycloidal wheel and the shaft	3 723 978 700
Between the internal cycloidal wheel and the shaft	3 135 975 900

Table 5. Viscous damping in bushings

Bushing	Damping [% critical damping]
Between the external sleeve and the ground	Analysis dependent (5, 20)
Between the internal sleeve and the internal pin	0
Between the external cycloidal wheel and the shaft	0
Between the internal cycloidal wheel and the shaft	0

4. DFT diagrams of the torque at the output shaft in the models excited with the oscillating torque at the input shaft (Table 1)

The angular velocity of the input shaft in the models excited with the oscillating input torque is not constant. Equilibrium of the gearbox is disturbed by the oscillating input torque, and there is gradual increase in the angular velocity during the analysis (Fig. 3). The DFT diagrams of the torque at the output shaft in the model excited with the oscillating input torque are shown in Fig. 4.
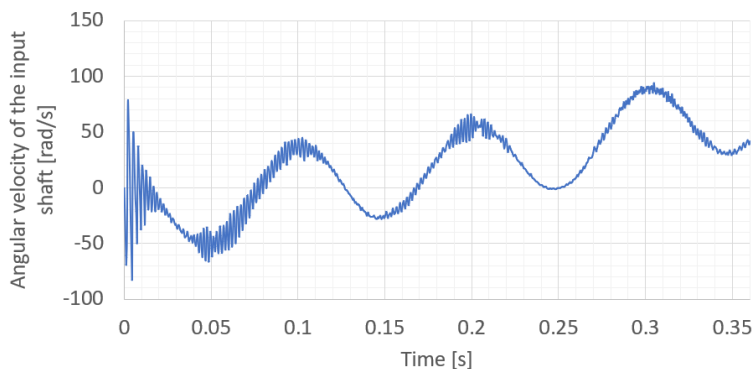

Fig. 3. The increase in the angular velocity of the input shaft due to the disturbed equilibrium
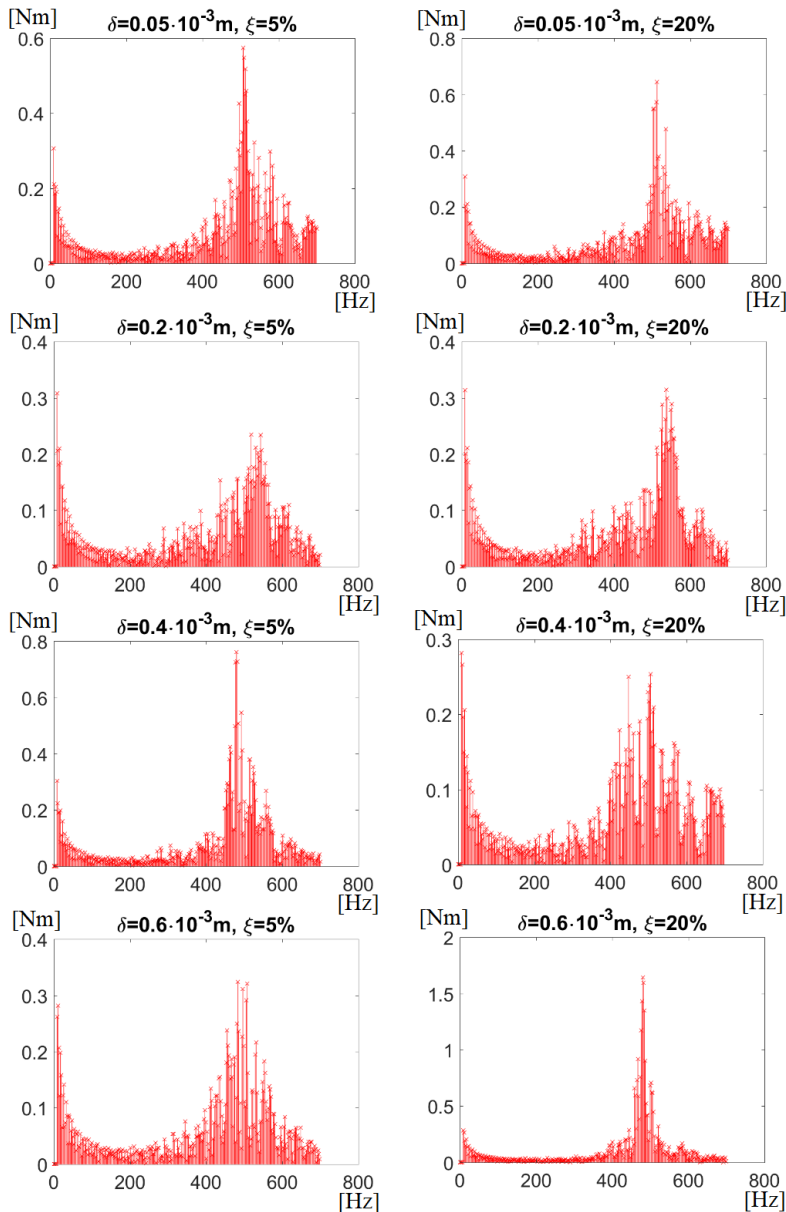between the input and the output torques

Fig. 4. The amplitude spectrum (output torque [Nm] versus frequency [Hz]) for different backlashes δ [m] and damping coefficients ξ [% of the critical damping]. The average value and the first three beans are zeroed. The model is excited with the oscillating input torque

The DFT diagrams were obtained using the FFT algorithm with Hamming window. In the Matlab software, the 8192-point FFTs were calculated and the right sides of the amplitude spectrums were shown. The beginning part of the output

torque time function was cut out by applying the Heaviside function (2) to eliminate the initial data disturbed by noise due to the contact parameters stabilization.

$$H(t) = \begin{cases} 1 & \text{for } t > 0, \\ 0 & \text{for } t < 0, \end{cases} \tag{2}$$

$$T'_{\text{OUT}} = H(t - 0.035s) \cdot T_{\text{OUT}}, \tag{3}$$

where: T_{OUT} – the output torque from the multibody dynamics analysis, $H(t)$ – the Heaviside function, T'_{OUT} – the output torque used in the DFT diagrams, t – time [s].

The use of the Heaviside function has an influence on the average value of the output torque (Table 6). If the zero part of the output torque is neglected, the average value should be approximately 22.5 Nm [5, 22]. In the DFT amplitude spectrums shown in Fig. 4, the average value and the first three beans were zeroed for the spectrum scaling and their values are presented in Table 6.

Table 6. The average value and the first three bins in the amplitude spectrum for the model excited with the oscillating input torque

Backlash and damping	Average value [Nm]	Freq. [Hz]	Amp. [Nm]	Freq. [Hz]	Amp. [Nm]	Freq. [Hz]	Amp. [Nm]
$\delta = 0.05 \cdot 10^{-3}$ m, $\xi = 5\%$	8.888	2.077	11.61	4.154	2.286	6.231	0.4637
$\delta = 0.2 \cdot 10^{-3}$ m, $\xi = 5\%$	8.875	2.073	11.62	4.146	2.308	6.218	0.4647
$\delta = 0.4 \cdot 10^{-3}$ m, $\xi = 5\%$	8.971	2.096	11.63	4.191	2.195	6.287	0.4668
$\delta = 0.6 \cdot 10^{-3}$ m, $\xi = 5\%$	9.284	2.168	11.65	4.337	1.839	6.505	0.4701
$\delta = 0.05 \cdot 10^{-3}$ m, $\xi = 20\%$	8.854	2.069	11.61	4.138	2.324	6.207	0.4647
$\delta = 0.2 \cdot 10^{-3}$ m, $\xi = 20\%$	8.878	2.074	11.62	4.148	2.303	6.223	0.4626
$\delta = 0.4 \cdot 10^{-3}$ m, $\xi = 20\%$	9.168	2.141	11.65	4.283	1.971	6.424	0.4752
$\delta = 0.6 \cdot 10^{-3}$ m, $\xi = 20\%$	9.175	2.144	11.65	4.288	1.958	6.432	0.4743

5. DFT diagrams of the torque at the output shaft in the model excited with constant angular velocity at the input shaft

In Fig. 5, the time courses of the output torque for different values of the backlash and the damping coefficients of the external sleeves' bushings are presented. The output torques were determined on the basis of forces acting on the

internal sleeves and sleeves' displacements. The diagrams do not show any linear dependence between the backlash and the amplitude of vibrations at the output shaft. In Fig. 5, the amplitude is increased for the high backlash ($0.6 \cdot 10^{-3}$ m). It could result from the fact that standard deviation of the impact-to-impact times is lower for the high backlash (see Fig. 12 in Section 6). Even distribution of the impact-to-impact times causes that excitation has a harmonic pattern. In cycloidal gearboxes, the loading state in a current iteration depends on previous iterations of loading. For a gearbox loaded by a different torque or having a different structure, the resulting dependencies will generally be different from the presented ones.
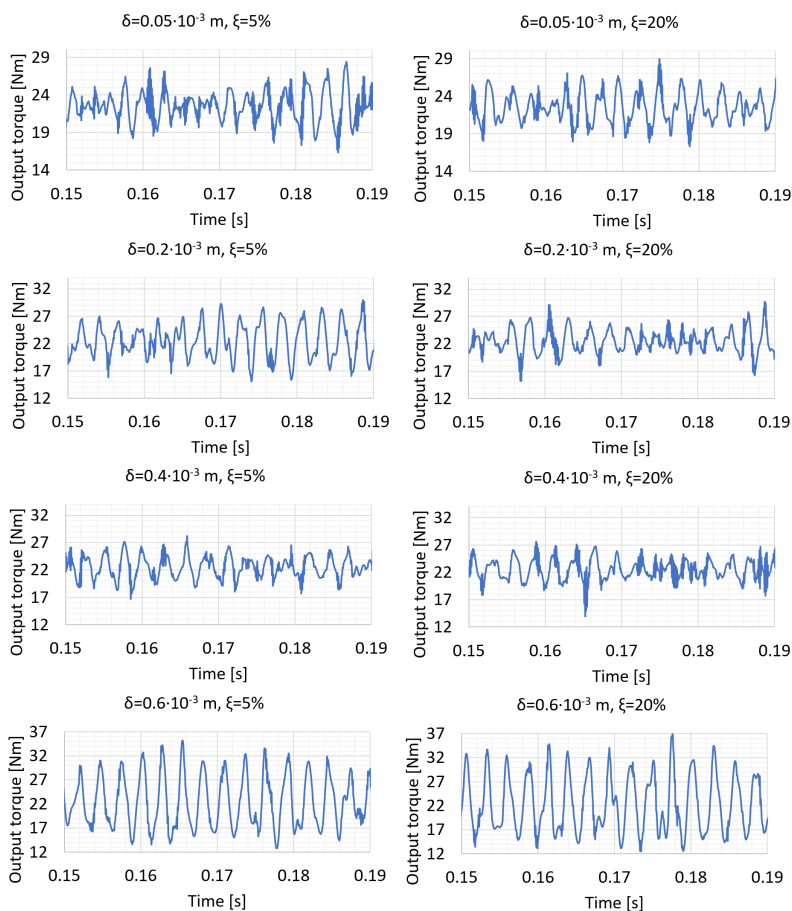
Fig. 5. Output torque [Nm] in the time domain [s] for the different values of the backlash δ [m] and external sleeves' bushings' damping coefficient ξ [% critical damping]

The DFT diagrams of the output torque in the models excited with constant angular velocity of the input shaft are presented in Fig. 6. In all of these diagrams,
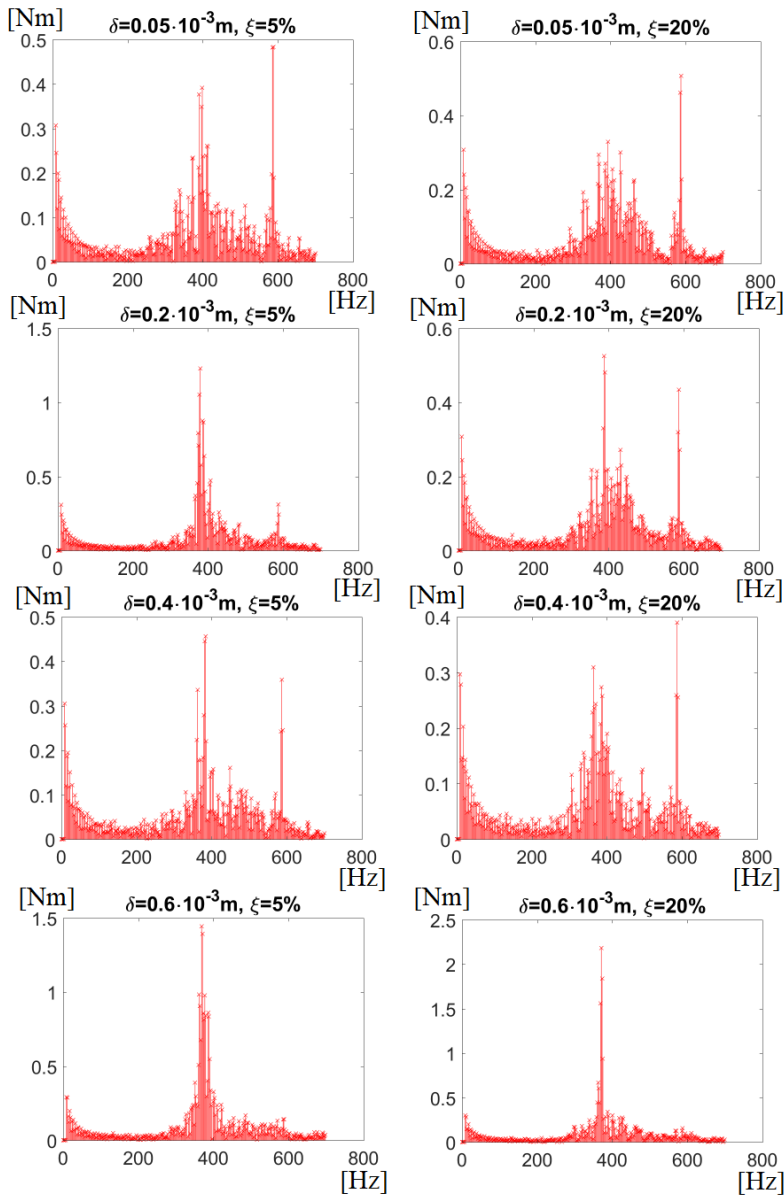
Fig. 6. Amplitude spectrum (the output torque [Nm] versus frequency [Hz]) for different backlashes δ [m] and damping coefficients ξ [% of the critical damping]. The average value and the first three beans are zeroed. The model with constant angular velocity of the input shaft

there are one or two amplitude peaks for the frequencies in the range of 380 Hz – 600 Hz. In the graphs, the average value and the first three bins are set to zero. The values of the zeroed beans are presented in Table 7.

Table 7. The average value and the first three bins in the amplitude spectrum for the model
with constant angular velocity of the input shaft

Backlash and damping	Average value [Nm]	Freq. [Hz]	Amp. [Nm]	Freq. [Hz]	Amp. [Nm]	Freq. [Hz]	Amp. [Nm]
$\delta = 0.05 \cdot 10^{-3}$ m, $\xi = 5\%$	8.906	2.077	11.64	4.154	2.286	6.231	0.4393
$\delta = 0.2 \cdot 10^{-3}$ m, $\xi = 5\%$	8.888	2.073	11.63	4.146	2.307	6.218	0.4396
$\delta = 0.4 \cdot 10^{-3}$ m, $\xi = 5\%$	8.987	2.096	11.65	4.191	2.193	6.287	0.4397
$\delta = 0.6 \cdot 10^{-3}$ m, $\xi = 5\%$	9.297	2.168	11.67	4.337	1.842	6.505	0.4336
$\delta = 0.05 \cdot 10^{-3}$ m, $\xi = 20\%$	8.873	2.069	11.63	4.138	2.325	6.207	0.4383
$\delta = 0.2 \cdot 10^{-3}$ m, $\xi = 20\%$	8.894	2.074	11.64	4.148	2.3	6.223	0.4395
$\delta = 0.4 \cdot 10^{-3}$ m, $\xi = 20\%$	9.182	2.141	11.66	4.283	1.97	6.424	0.4364
$\delta = 0.6 \cdot 10^{-3}$ m, $\xi = 20\%$	9.193	2.144	11.67	4.288	1.959	6.432	0.4377

6. The analysis of the impact-to-impact times between the cycloidal wheel and the external sleeves for different values of backlash and different damping coefficients

Backlash in the model leads to serial impacts of the cycloidal wheel into the external sleeves. The impact-to-impact times were analyzed in the models with different backlash values. The cycloidal wheel in the positions of two consecutive impacts is presented in Fig. 7.
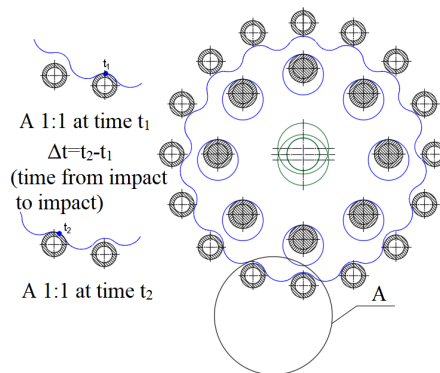

Fig. 7. Impact-to-impact time Δt for the cycloidal wheel
and the external sleeves

The DFT diagrams for the combined function, which consists of sine functions with half-periods equal to the times between impacts of the cycloidal gear into external sleeves (Fig. 8) are presented in Fig. 9. Fig. 9 shows that the width of the amplitude spectrum decreases with the increase in the backlash.
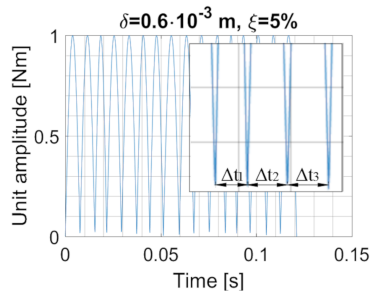
Fig. 8. The function combined from sine functions with half-periods equal to the times
($\Delta t_1, \Delta t_2, \Delta t_3, \dots$) from impact to impact for the cycloidal gear and the external sleeves
(unit amplitude [Nm] versus time [s]) for the backlash $\delta = 0.6 \cdot 10^{-3}$ m and damping
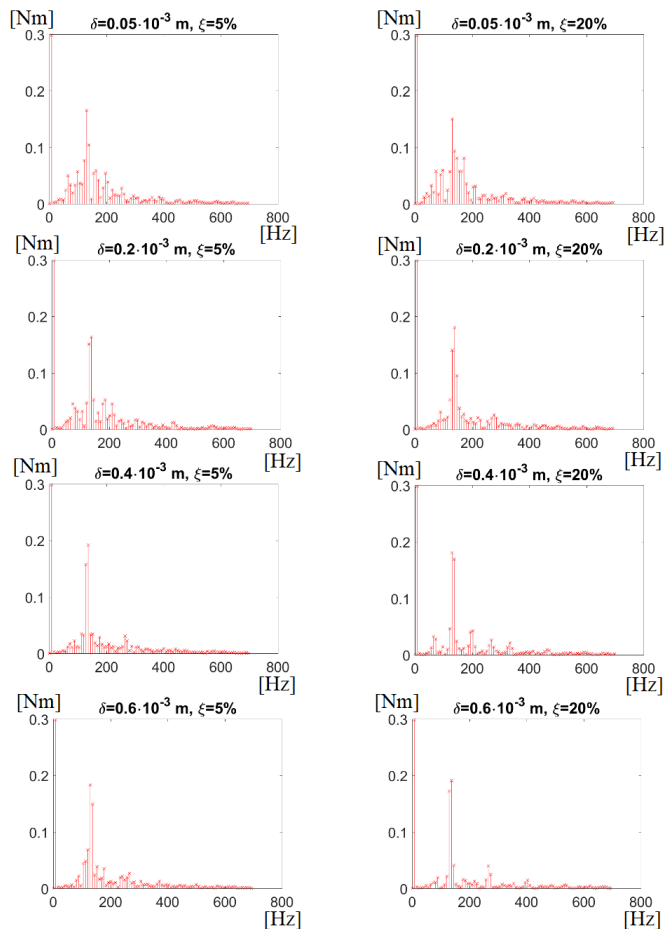coefficient $\xi = 5\%$ of the critical damping

Fig. 9. Amplitude spectrum (amplitude [Nm] versus frequency [Hz]) for the combined functions
calculated for different backlashes δ [m] and damping coefficients ξ [% of the critical damping]. The
impact-to-impact times determined in the model with constant angular velocity of the input shaft

The impact-to-impact times determined in the model with constant angular velocity of the input shaft were compared for different values of the backlash: in Fig. 10 for 5% damping and in Fig. 11 for 20% damping in the external sleeves' bushings. The damping values are theoretical. Two values of damping were assumed to compare the obtained results: low (5% of the critical damping), which was typical for the steel constructions, and a high value of damping (20% of the critical damping). These values of damping were not obtained from an analysis, they cannot be found in the data sources, either. Standard deviations of the time increments are shown in Fig. 12.
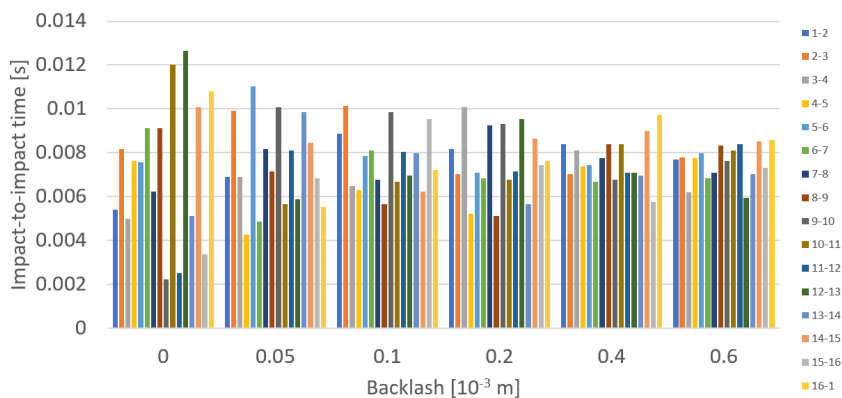
Fig. 10. Impact-to-impact times for different backlash values in the model with constant angular velocity of the input shaft. The damping coefficient in the external sleeves' bushings is 5% of the critical damping
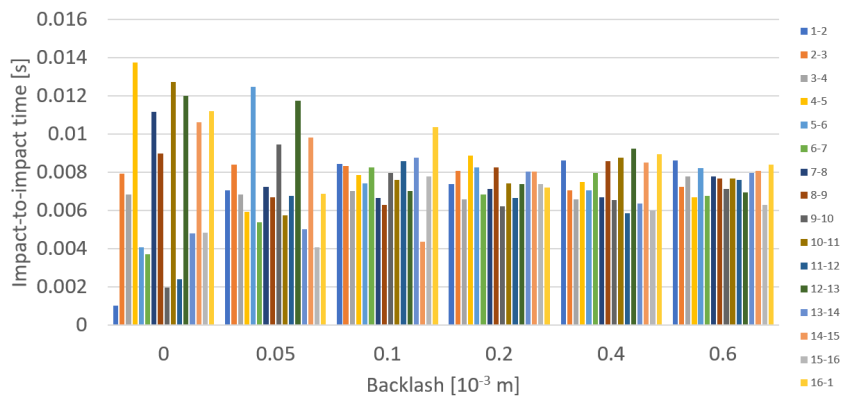

Fig. 11. Impact-to-impact times for different backlash values in the model with constant angular velocity of the input shaft. The damping coefficient in the external sleeves' bushings is 20% of the critical damping
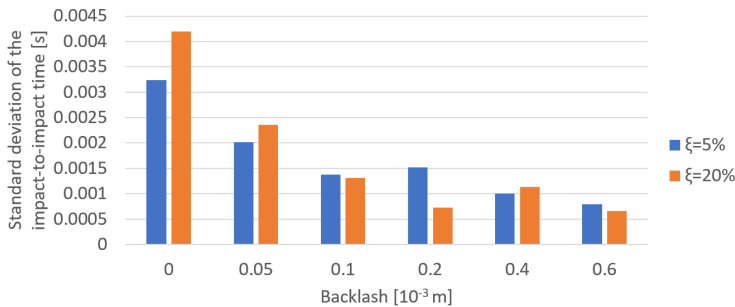
Fig. 12. Standard deviations of the impact to impact times in the model with constant angular velocity of the input shaft for two damping coefficients in the external sleeves' bushings: 5% and 20% of the critical damping

7. The number of the external sleeves working at the same time determined on the basis of the time course of the contact forces between the external cycloidal wheel and the external sleeves

In this section, the number of the external sleeves being in contact at the same time was investigated as a function of the backlash. In the MSC Adams, the request was programmed, with the aim of storing the contact status on the basis of the contact force components. The contact status is the number of the external sleeve which is in contact with the external cycloidal gear. During the contact, the force components are saved. When the horizontal component of the force is greater than 2 N, the contact status assumes the value equal to the sleeve's number. In the opposite case, its value is zero. When the vertical component of the force is greater than 2 N, the contact status attains the value equal to the sleeve's number increased by 0.5, otherwise its value is zero. The small threshold value of 2 N was used to filter out numerical errors and negligible values which appear during the analysis. The values of contact status for various backlash values are shown in Fig. 13.

8. Discussion of results

In this article, the influence of backlash on the output torque spectrum was investigated. The amplitude spectrums of the output torque in the presented models are different depending on the methods of excitation. For both methods of excitation shown in Figs 4 and 6 one can see amplitude peaks at frequencies in the range of 380 Hz – 600 Hz. These amplitude peaks (Fig. 14a) originate from the oscillations of the output torque (Fig. 14b), which are caused by the oscillating angular velocity of the output shaft.

The frequency of the angular velocity of the output shaft calculated in the analysis for the model with the backlash of $0.1 \cdot 10^{-3}$ m is 384 Hz, which corresponds
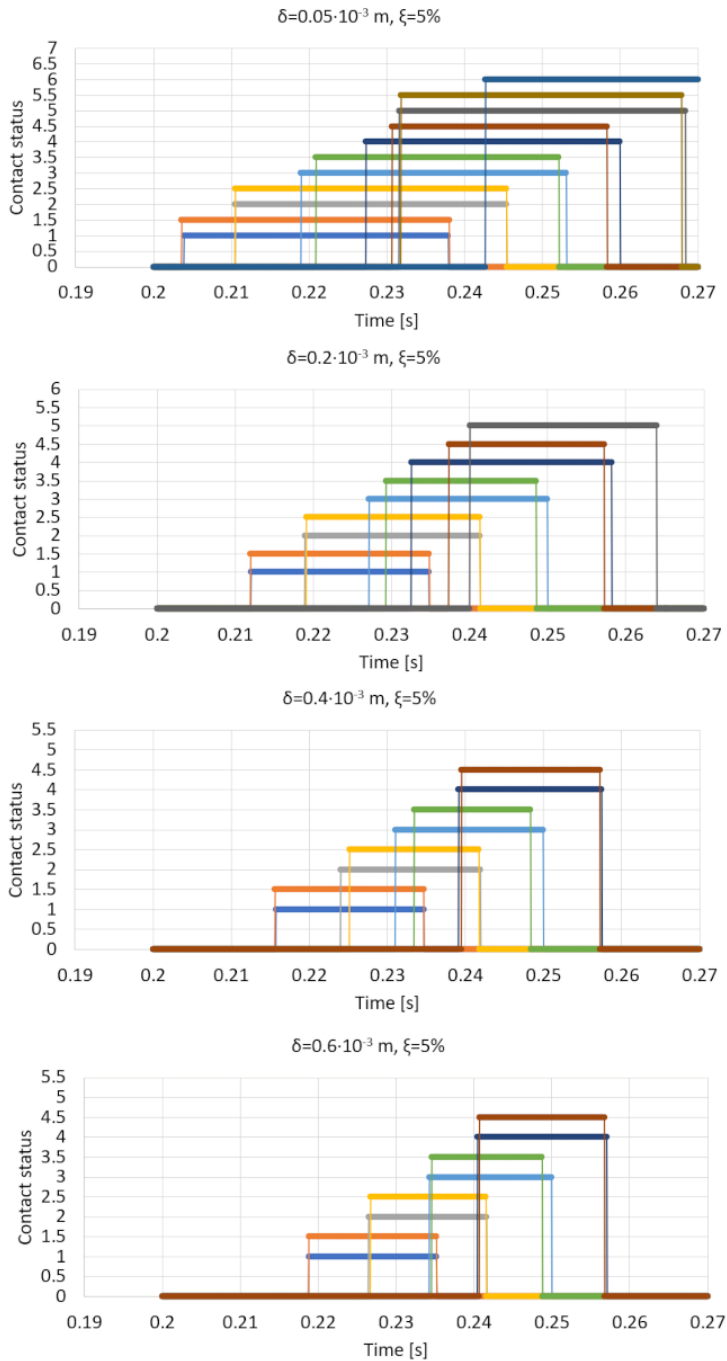
Fig. 13. The contact status for different values of the backlash δ [m].
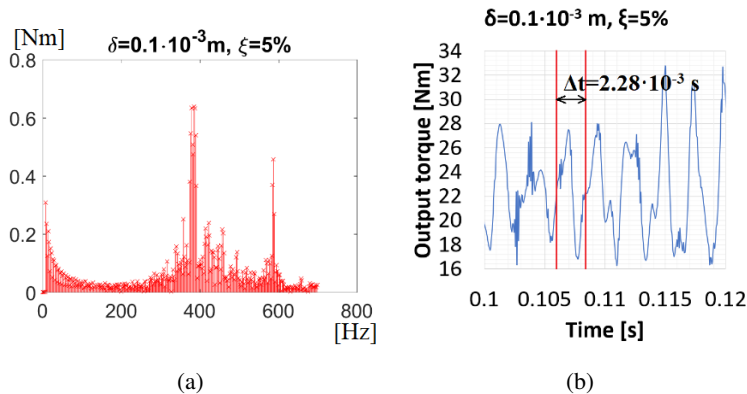The damping coefficient is 5% of the critical damping

Fig. 14. Amplitude spectrum of the output torque (a) and the output torque in the time domain (b). The average value and the first three frequency bins were zeroed for a proper image scaling

to the frequency of the first peak (Fig. 14a). The second peak originates from the velocity of the external sleeve at the time of contact deformation. Oscillations of the selected component of the linear velocity of the selected external sleeve are shown in Fig. 15. The amplitude spectrum (Fig. 15a) shows two peaks in the positions similar to the peaks in Fig. 14a.

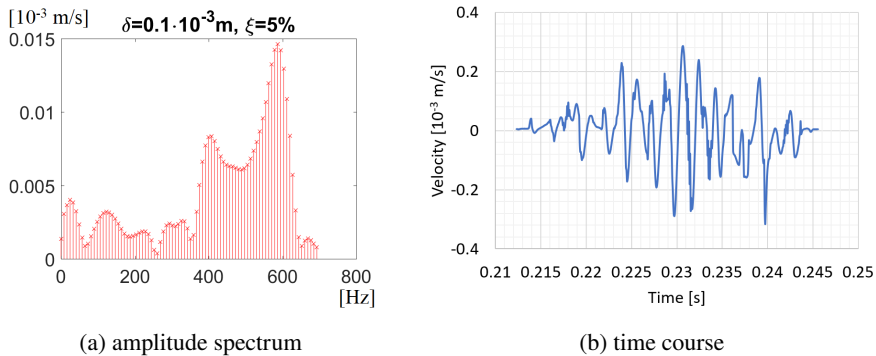

(a) amplitude spectrum
(b) time course

Fig. 15. Linear velocity of the selected external sleeve at the time of contact with the cycloidal wheel

The frequency of the output torque fluctuation calculated for the selected period is ≈439 Hz (Fig. 14b). The time course of the output torque in Fig. 14b is modulated by the contact interactions, which is shown in Fig. 15b on the example of velocity oscillations.

The natural frequencies depend on the stiffness and mass of the given part. If the natural vibrations of the component part are excited, it can be seen in the output torque spectrum in the form of the spectral component at the frequency equal to natural frequency of that part or its multiple. These values for the internal and external sleeves are 3597 Hz and 14 380 Hz, respectively. Similar values of

the natural frequencies were obtained in the modal analysis in the MSC Adams, but these components were not analyzed in the considered amplitude spectrums (Figs 4, 6, 9 and 14).

For verification purposes, the impact-to-impact times between the cycloidal wheel and the external sleeves were computed in the multibody dynamics analysis. The amplitude spectrums of the combined function containing half-periods equal to the impact-to-impact times are narrower for the high values of backlash and wider for the small backlashes. It can be also seen in Figs 10–12 that the standard deviation of the impact-to-impact times decreases with the increase in the backlash. It can be influenced by the method of contact modeling [23, 24] in the MSC Adams. According to [23], this software uses triangulation in the representation of contacting surfaces. The parameters of the user interface, which can determine the contact modeling are penetration depth and contact stiffness. The penetration depth defines the value of the distance needed to obtain full damping. Unfortunately, it is difficult to predict the distance at which the contact of two bodies is detected.

The first frequencies of beans in the amplitude spectrums of the combined functions are equal the excitation frequency (≈ 8.33 Hz, ≈ 500 RPM). The following peaks of significant values are in the frequency range of 129–138.5 Hz and their frequencies are equal to 16 (the number of external sleeves) times the excitation frequency.

In Fig. 5, the output torques in the time domain are presented for different values of backlash. The time courses for the backlash of $0.6 \cdot 10^{-3}$ m have greater amplitudes compared to those of other backlashes. As it was presented in [22], the natural frequencies of the gearbox change with the position of the cycloidal wheels. The gearbox passes through the vibration zones with increased amplitude. In this example, the wide zone of increase in the amplitude may result from the harmonic excitation. The impact-to-impact times have more even distribution for the high values of backlash, which can excite high amplitude vibrations.

In Fig. 13, the contact status for different values of the backlash is shown. For the greater backlash, less lobes enter in contact at the same time. For the backlash of $\delta = 0.05 \cdot 10^{-3}$ m, 5 lobes are in contact, and for $\delta = 0.6 \cdot 10^{-3}$ m – only 3 lobes are in contact at the same time. It can influence natural frequencies of the cycloidal gearbox. If the cycloidal wheel is in contact with 3 external sleeves and not with 5, the structure has lower stiffness. In the model with $\delta = 0.6 \cdot 10^{-3}$ m backlash, the modal analysis in the MSC Adams showed natural frequencies in the range of 6.17 Hz – 980.8 Hz, which are lower than the natural frequency of the internal sleeve vibrations (3594 Hz).

9. Conclusions

Summing up the results, the backlash in the cycloidal gearbox has significant influence on the spectrum of the output torque. Unfortunately, the dependencies between the components of the spectrum and the backlash cannot be expressed by

linear equations, especially when the vibrations of the output torque in the range of (380 Hz – 600 Hz) are considered. In the cycloidal gearboxes, the current value of the output torque depends on previous cycles of loading. Generally, the results obtained for a given gearbox model will not show similar dependencies for the gearboxes with different ratios, geometry or loading state.

The gradual dependence can be found in the spectrum determined for the combined sine functions containing impact-to-impact times. The spectrum is narrower for high values of backlash, which could be caused by the harmonic excitation due to even distribution of the impact-to-impact times.

Acknowledgements

References

[1] M. Blagojević, M. Matejić, and N. Kostić. Dynamic behaviour of a two-stage cycloidal speed reducer of a new design concept. *Tehnički Vjesnik*, 25(2):291–298, 2018, doi: 10.17559/TV-20160530144431.

[2] M. Wikło, R. Król, K. Olejarczyk, and K. Kołodziejczyk. Output torque ripple for a cycloidal gear train. *Proceedings of the Institution of Mechanical Engineers, Part C: Journal of Mechanical Engineering Science*, 233(21–22):7270–7281, 2019, doi: 10.1177/0954406219841656.

[3] N. Kumar, V. Kosse, and A. Oloyede. A new method to estimate effective elastic torsional compliance of single-stage Cycloidal drives. *Mechanism and Machine Theory*, 105:185–198, 2016, doi: 10.1016/j.mechmachtheory.2016.06.023.

[4] C.F. Hsieh. The effect on dynamics of using a new transmission design for eccentric speed reducers. *Mechanism and Machine Theory*, 80:1–16, 2014, doi: 10.1016/ j.mechmachtheory. 2014.04.020.

[5] R. Król. Kinematics and dynamics of the two stage cycloidal gearbox. *AUTOBUSY – Technika, Eksploatacja, Systemy Transportowe*, 19(6):523–527, 2018, doi: 10.24136/atest.2018.125.

[6] K.S. Lin, K.Y. Chan, and J.J. Lee. Kinematic error analysis and tolerance allocation of cycloidal gear reducers. *Mechanism and Machine Theory*, 124:73–91, 2018, doi: 10.1016/ j.mechmachtheory.2017.12.028.

[7] L.X. Xu, B.K. Chen, and C.Y. Li. Dynamic modelling and contact analysis of bearing-cycloid-pinwheel transmission mechanisms used in joint rotate vector reducers. *Mechanism and Machine Theory*, 137:432–458, 2019, doi: 10.1016/j.mechmachtheory.2019.03.035.

[8] D.C.H. Yang and J.G. Blanche. Design and application guidelines for cycloid drives with machining tolerances. *Mechanism and Machine Theory*, 25(5):487–501, 1990, doi: 10.1016/0094-114X(90)90064-Q.

[9] J.W. Sensinger. Unified approach to cycloid drive profile, stress, and efficiency optimization. *Journal of Mechanical Design*, 132(2):024503, 2010, doi: 10.1115/1.4000832.

[10] Y. Li, K. Feng, X. Liang, and M.J. Zuo. A fault diagnosis method for planetary gearboxes under non-stationary working conditions using improved Vold-Kalman filter and multi-scale sample entropy. *Journal of Sound and Vibration*, 439:271–286, 2019, doi: 10.1016/j.jsv.2018.09.054.

[11] Z.Y. Ren, S.M. Mao, W.C. Guo, and Z. Guo. Tooth modification and dynamic performance of the cycloidal drive. *Mechanical Systems and Signal Processing*, 85:857–866, 2017, doi: 10.1016/j.ymssp.2016.09.029.

[12] L.X. Xu and Y.H. Yang. Dynamic modeling and contact analysis of a cycloid-pin gear mechanism with a turning arm cylindrical roller bearing. *Mechanism and Machine Theory*, 104:327–349, 2016, doi: 10.1016/j.mechmachtheory.2016.06.018.

[13] S. Schmidt, P.S. Heyns, and J.P. de Villiers. A novelty detection diagnostic methodology for gearboxes operating under fluctuating operating conditions using probabilistic techniques, *Mechanical Systems and Signal Processing*, 100:152–166, 2018, doi: 10.1016/ j.ymssp. 2017.07.032.

[14] Y. Lei, D. Han, J. Lin, and Z. He. Planetary gearbox fault diagnosis using an adaptive stochastic resonance method. *Mechanical Systems and Signal Processing*, 38(1):113–124, 2013, doi: 10.1016/j.ymssp.2012.06.021.

[15] Y. Chen, X. Liang, and M.J. Zuo. Sparse time series modeling of the baseline vibration from a gearbox under time-varying speed condition. *Mechanical Systems and Signal Processing*, 134:106342, 2019, doi: 10.1016/j.ymssp.2019.106342.

[16] G. D'Elia, E. Mucchi, and M. Cocconcelli. On the identification of the angular position of gears for the diagnostics of planetary gearboxes. *Mechanical Systems and Signal Processing*, 83:305–320, 2017, doi: 10.1016/j.ymssp.2016.06.016.

[17] X. Chen and Z. Feng. Time-frequency space vector modulus analysis of motor current for planetary gearbox fault diagnosis under variable speed conditions. *Mechanical Systems and Signal Processing*, 121:636–654, 2019, doi: 10.1016/j.ymssp.2018.11.049.

[18] S. Schmidt, P.S. Heyns, and K.C. Gryllias. A methodology using the spectral coherence and healthy historical data to perform gearbox fault diagnosis under varying operating conditions. *Applied Acoustics*, 158:107038, 2020, doi: 10.1016/j.apacoust.2019.107038.

[19] D. Zhang and D. Yu. Multi-fault diagnosis of gearbox based on resonance-based signal sparse decomposition and comb filter. *Measurement*, 103:361–369, 2017, doi: 10.1016/j.measurement.2017.03.006.

[20] C. Wang, H. Li, J. Ou, R. Hu, S. Hu, and A. Liu. Identification of planetary gearbox weak compound fault based on parallel dual-parameter optimized resonance sparse decomposition and improved MOMEDA. *Measurement*, 165:108079, 2020, doi: 10.1016/j.measurement.2020.108079.

[21] W. Teng, X. Ding, H. Cheng, C. Han, Y. Liu, and H. Mu. Compound faults diagnosis and analysis for a wind turbine gearbox via a novel vibration model and empirical wavelet transform. *Renewable Energy*, 136:393–402, 2019, doi: 10.1016/j.renene.2018.12.094.

[22] R. Król. Resonance phenomenon in the single stage cycloidal gearbox. Analysis of vibrations at the output shaft as a function of the external sleeves stiffness. *Archive of Mechanical Engineering*, 68(3):303–320, 2021, doi: 10.24425/ame.2021.137050.

[23] MSC Software. MSC Adams Solver Documentation.

[24] MSC Software. MSC Adams View Documentation.